Utilization of Deep Learning Methods for Automatic Reconstruction of Quantitative Phase Images in Non-Telecentric Digital Holographic Microscopy

Brian Bogue-Jimenez[1,a], Shashwat Patra[1,b], Carlos Trujillo[2,c], and Ana Doblas[1,d]

Author Affiliations
[1]*University of Memphis, Department of Electrical and Computer Engineering, Memphis, TN, USA*
[2]*Universidad EAFIT, School of Applied Sciences and Engineering, Medellin, Colombia*

[a)] *bbgjmnez@memphis.edu*
[b)] *spatra@memphis.edu*
[c)] *catrujilla@eafit.edu.co*
[d)] *Corresponding author: adoblas@memphis.edu*

Keywords. Quantitative Phase Imaging, Digital Holographic Microscopy, Compensated Phase Maps, Artificial Intelligence, Deep Learning, Automation

Abstract. We have investigated a learning-based model to automatically and accurately reconstruct quantitative phase images from holograms captured by a digital holographic microscope (DHM) operating in non-telecentric regime. Reported automatic reconstruction methods for non-telecentric DHM systems are time consuming, and their performance is highly dependent on the sample field of view and the optical configuration of the system. In a recent work, our research group proposed a generative adversarial network to accurately reconstruct quantitative phase images with minimum phase distortions from a hologram recorded by telecentric-based DHM systems. In this contribution, we have analyzed the performance of such a network to fully compensate and reconstruct holograms recorded by non-telecentric DHM systems without the need for any manual computational processing. This learning-based model was trained and validated using simulated hologram paired with phase image of HeLa kinases.

INTRODUCTION

Optical microscopy is an essential tool used in the field of medical research for imaging specimens invisible to the human eye. One optical imaging technique commonly implemented in microscopy is holography, invented by Dennis Gabor in 1948 [1]. Holography creates quantitative phase images leveraging the principle of superposition of two beams to create an interference pattern, commonly referred to as a hologram [2,3]. The advantage of holography compared to other optical imaging techniques is that both amplitude and phase distributions of an arbitrary object are encoded in the intensity distribution of the hologram.

Digital holographic microscopy (DHM) is an important implementation of quantitative phase imaging (QPI), as it is capable of imaging biological samples that could not be imaged using conventional bright-field microscopy. This is because most biological samples exhibit low optical scattering, so they become transparent in conventional systems, leading to the need for chemical pre-processing (i.e., staining) of the specimen in order to generate fluorescent images. In contrast, DHM systems rely solely on phase shifts introduced by the specimen which get encoded in the holograms. After undergoing a reconstruction process, the amplitude and phase distributions of the sample can be retrieved from the hologram image, generating three-dimensional (3-D) images of the specimen under research [4,5]. An additional advantage is that this 3-D image is obtained in a single shot, eliminating the need for

slow axial scanning through the sample. This makes DHM perfect for label-free live-cell imaging, where characterization of the biological sample under question over time is desired.

The reconstruction process is highly dependent on the optical configuration of the DHM system. One important distinction between DHM optical configurations is if the DHM systems operate in telecentric regime or not. Single-shot DHM systems operating in the telecentric regime only require the compensation of the interference angle between the object and reference waves. Oppositely, non-telecentric DHM systems should compensate for the spherical phase factor recognized in DHM and associated with a non-telecentric imaging system [6,7,8,9]. Although telecentric-based DHM systems are intrinsically linear shift-invariant imaging systems, requiring minimum computational steps to provide accurate quantitative phase images [8,9], the DHM community has not accepted them. Generally, DHM systems follow a non-telecentric configuration, so the phase distribution of the object is distorted by a spherical term, requiring the precise correction of such term to provide quantitative phase imaging. This spherical term can be corrected computationally by accurately finding its center and radius of curvature, generating a conjugated spherical aberration (a spherical aberration with the same parameters but opposite phase), then multiplying it to the uncorrected phase image to cancel the spherical term out. In 2017, Min et al. aimed to automatically determine these parameters from the Fourier spectrum of the recorded hologram with minimum user input [10]. However, the implementation of this approach can be computationally expensive and might not always reconstruct phase images without distortions. Recently, a Generative Adversarial Network (cGAN) model has been validated to reconstruct phase images with minimum phase distortions from a hologram recorded by DHM systems operating at the telecentric regime [11]. In this paper, we expand on this work by implementing the cGAN model for automatically correcting and reconstructing images from holograms obtained with non-telecentric DHM systems. The model was trained and tested on a simulated dataset based on non-telecentric DHM systems to validate its accuracy in reconstructing accurate phase images.

METHODOLOGY

Section 2.1: Simulated Dataset

We simulated an off-axis Mach-Zehnder DHM system shown in Fig. 1, which is a modified Mach-Zehnder interferometer. The hologram recorded by the sensor surface located at the image plane of the microscopic imaging system is given by the equation:

$$h(x,y) = |u(x,y)|^2 + |r(x,y)|^2 + u(x,y)r^*(x,y) + r^*(x,y)r(x,y) \tag{1}$$

where (x,y) are the lateral spatial coordinates. The complex object distribution u(x, y) is given by,

$$u(x,y) = \frac{1}{M^2}\exp\left[\, i\frac{k}{2C}(x^2+y^2)\right] \bullet\ o\ \left[\frac{x}{M},\frac{y}{M}\right] \otimes_2 P\left(\frac{x}{\lambda f_{TL}},\frac{y}{\lambda f_{TL}}\right)\Bigg], \tag{2}$$

where M is the lateral magnification factor, k is the wave number that depends on the illumination's wavelength (λ) via $k = 2\pi/\lambda$ and $C = f_{\mathrm{TL}}^2/[f_{\mathrm{TL}} - d]$ is the radius of curvature of the spherical phase factor in Eq. (2) associated with the use of a non-telecentric geometry (i.e., the distance between the aperture of the microscope objective (MO) lens and the tube lens (TL) differs from the focal length of the TL, ($d \neq f_{\mathrm{TL}}$) for the optical microscope [8,9]. In Eq. (1), $r(x, y)$ is the tilted uniform reference beam,

$$r(x,y) = \quad \overline{I_R}\exp\left[\mathrm{j}k\left(x \bullet \sin\theta_x + y \bullet \sin\theta_y\right)\right], \tag{3}$$

where I_R is the intensity of the reference wave and θ_x and θ_y are the angles at which the reference beam interferes with the object wave before impinging on the image sensor. For off-axis DHM systems, the angle between both object and reference waves is such as there is no overlap between the different terms of the hologram's spectrum, enabling the spatial filtering of the object's frequencies using a single image [12].

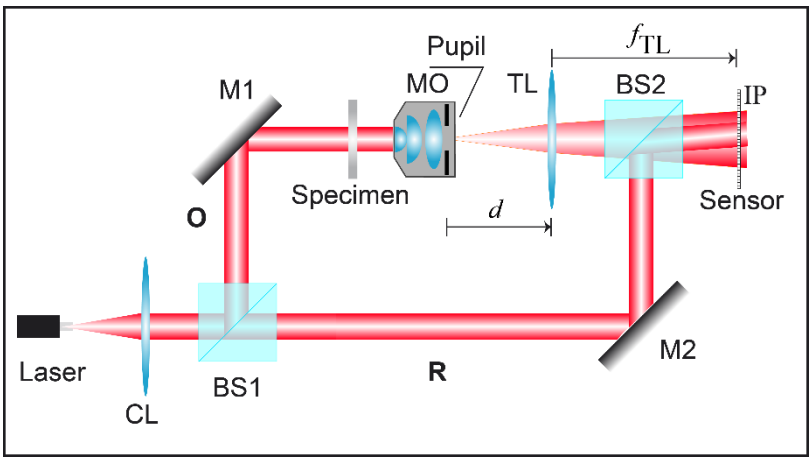

FIGURE 1. Optical configuration of an off-axis DHM system based on a modified Mach-Zenhder interferometer. In a general case, the microscopic objective (MO) lens and the tube lens (TL) are arranged in non-telecentric mode ($d \neq f_{TL}$). The remaining components of the system are denoted as: CL, converging lens; BS, beamsplitter; IP, image plane; M, mirror; O, object wave; R, reference wave.

Using these equations, we created holograms (Fig. 2a) by substituting $o\left(\frac{x}{M},\frac{y}{M}\right)$ with the grayscale images from the Kinome Atlas dataset [13]. We chose this dataset as HeLa cells are widely imaged by DHM systems making our simulated dataset like what would be expected from experimental samples. In our simulated dataset, we used the following parameters: $\lambda = 633$ nm, $f_{TL} = 200$ mm, and a spherical term with a random radius of curvature (C) value chosen from 3500 mm, 4000 mm, and 5000 mm. Note that these radii of curvatures correspond to a d-value of 188.6 mm, 190 mm, and 192 mm, respectively. Arbitrarily, we have considered that the center of the spherical aberration is located at top left corner (Fig. 2c). If the DHM system operates in the telecentric regime, the reconstruction method that is used involves the Fourier filtering of the object frequencies from the hologram's spectrum and the phase compensation of the tilting angle between the object and references beams due to the off-axis configuration. Nonetheless, the reconstructed phase maps after applying these two processes in a non-telecentric DHM system shows a ring-like structure superimposed over the HeLa cells, whose edges have been highlighted in Fig. 2c. Note that the magnitude of the spherical aberration is much greater than the phase from the optically thin cells. These structured patterns are inherited from the non-telecentric configuration, making the DHM system shift-variant (i.e., the accuracy of the phase measurements is highly dependent on the position of the sample within the imaged field of view). Therefore, this spherical aberration must be eliminated to provide accurate phase images via *a-posteriori* computational approaches [14,15,16], a double-exposure technique [17] or introducing a twin-imaging system [18]. The main objective of this study is the reconstruction of quantitative phase images directly from non-telecentric DHM holograms using a cGAN learning-based model. The non-telecentric DHM dataset is composed by pairing holograms [Fig. 2a] with ground-truth phase images [Fig. 2d]. Figure 2 shows three examples of our simulated dataset for the same ground-truth HeLa image and with different spherical phase term (i.e., different distances between the MO and TL lenses). Randomly assigning three different values for the curvature was done to ensure that the trained network can generalize its reconstruction ability. Note that the three holograms in Fig. 2a look alike; the difference in the spherical phase term is not observable from the hologram even though zooming in a region of the hologram distribution [Fig. 2b].

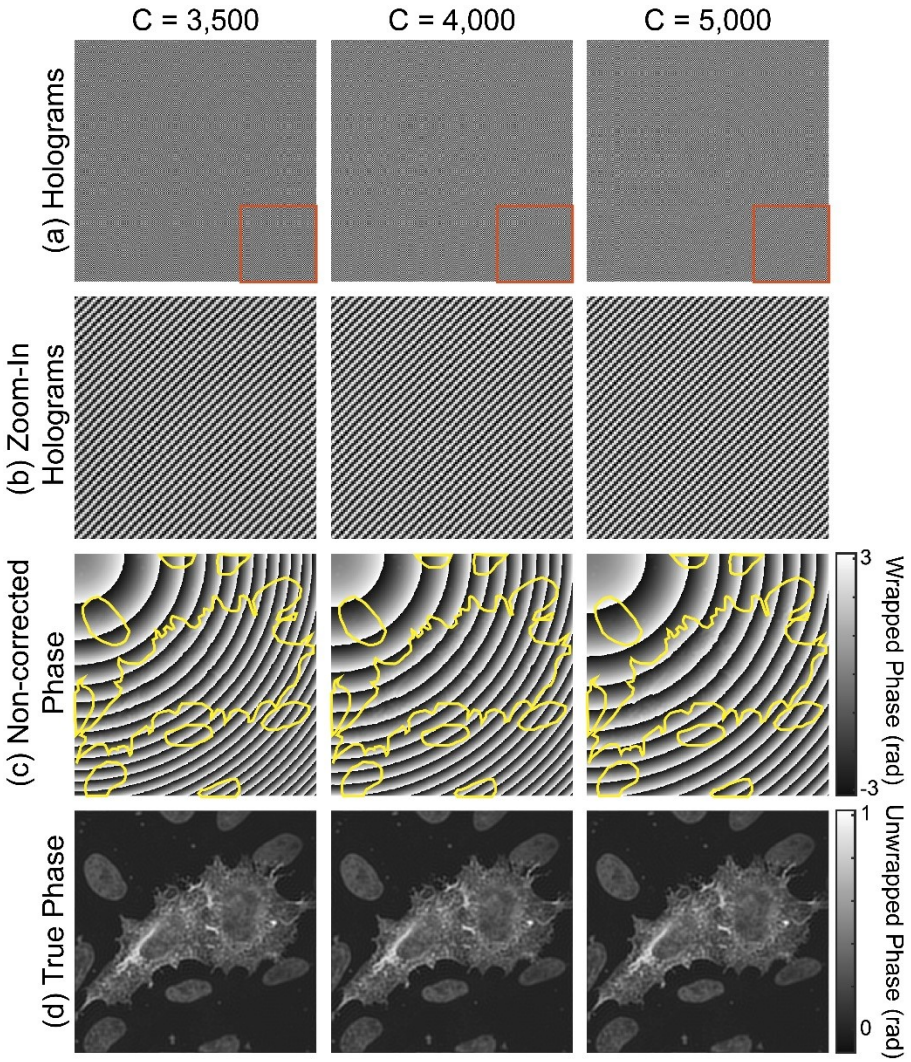

FIGURE 2. Illustration of the non-telecentric DHM dataset using HeLa cells from the Kinome Atlas dataset: (a) Input simulated off-axis holograms; (b) their respective reconstructed phase maps distorted by the spherical phase factor introduced by the non-telecentric configuration; and (c) the ground-truth phase maps without any undesired distortion.

Section 2.2: Conditional Generative Adversarial Network

The cGAN model (shown in Fig. 3) that we have used has been shown to work well with the general image-to-image translation tasks. The model comprises two neural networks competing with one another. The generative network inputs the non-telecentric hologram and the ground truth image and outputs a predicted phase image. On the other hand, the discriminator network determines whether the predicted phase image looks real or fake. Traditional deep learning models minimize loss functions that compare the network output to the ground truth pixel-wise. The most common of these functions are the mean square error and the mean absolute error. These loss functions have been shown to only pass low-frequency information through the network producing blurry results. In cGANs, the result of the discriminator network loss supplements the generator's loss function, allowing it to pass high-frequency information [19] better. The cGAN we implemented for reconstructing our phase images is based on the pix2pix paper [19], as shown in Fig. 3.

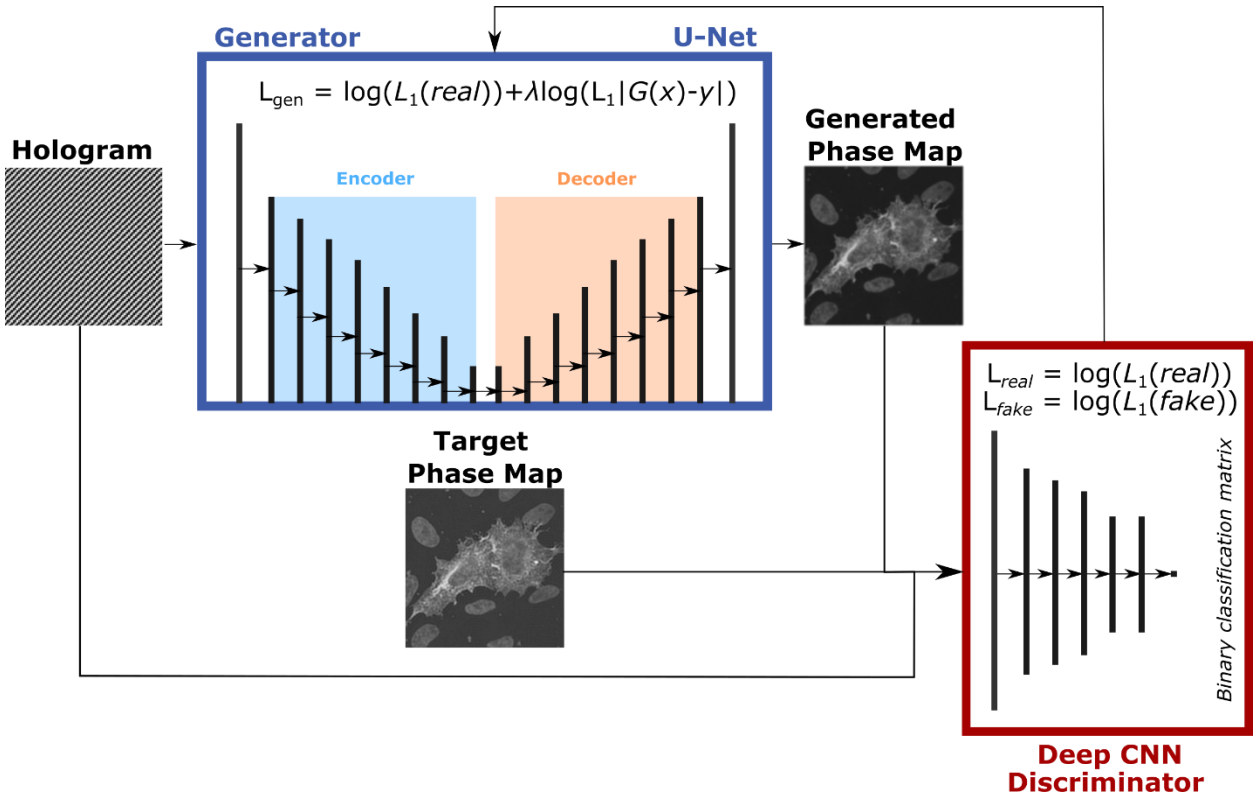

FIGURE 3. cGAN architecture used in Castaneda *et al.* [11]

The generator is a convolutional neural network (CNN) model called a U-net [20], and the discriminator is a CNN model coined by Isola et al. as PatchGAN [18]. The PatchGAN architecture determines whether arbitrary N×N patches of an image are real or fake. Smaller patches require less parameters, so the network runs and trains faster. The generative model is trained with the loss function being a weighted sum of the mean absolute error (MAE) between the predicted phase and ground truth and binary cross entropy loss from the discriminator. Our cGAN was trained with the MAE having a weight of 100, the discriminator loss having a weight of 1, patch sizes of 70×70, and used the Adam optimizer with a learning rate of 0.0002. The metric we used to determine the accuracy of our model was the peak signal to noise ratio (PSNR) which is defined as

$$\mathrm{PSNR} = \log_{10} \frac{\mathrm{MAX}_I^2}{\mathrm{MSE}}, \tag{4}$$

where MAX_I is the maximum intensity value of the image and MSE is the mean squared error. We have applied an 80:20 dataset split between training and validation, respectively.

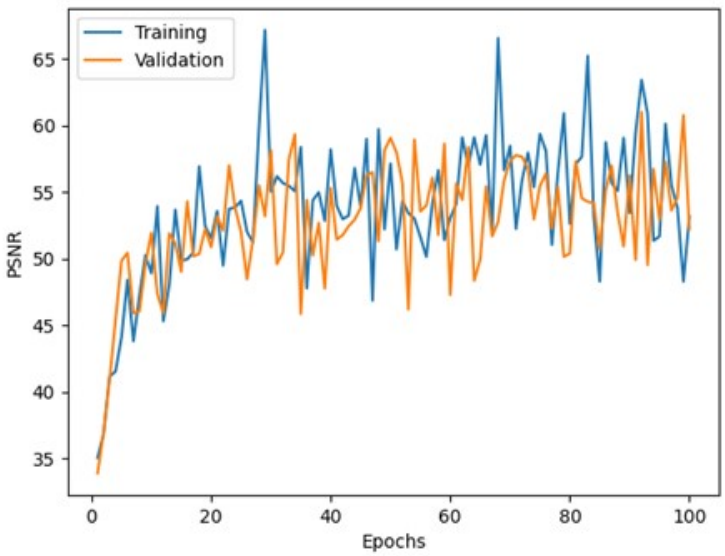

FIGURE 4. Peak Signal-to-Noise Ratio (PSNR) vs Number of Epochs of the Training and Testing datasets.

RESULTS AND DISCUSSIONS

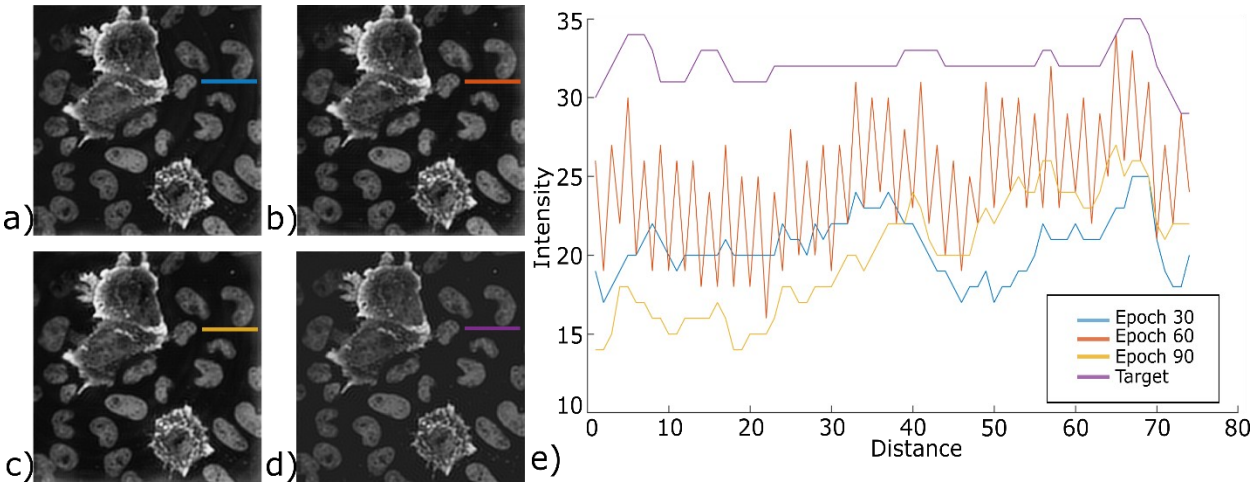

FIGURE 5. Generated phase images by the trained cGAN learning-based model at different epochs (a) 30, (b) 60, and (c) 90. The true phase image is shown in panel (d). Panel (e) plots the intensity distribution of the phase images (a)-(d).

To quantify the performance of the cGAN model, we graphed the PSNR value at each epoch of the training. Figure 4 shows the average PSNR of 15 random images in the training and testing dataset for each epoch. We see that the PSNR values fluctuate, but, overally, the PSNR value kept quite constant after epoch 30. In Figure 5a-c, we show the generated phase images from epoch 30, 60 and 90. For comparison purposes, the true phase image is shown in Fig. 5d. We observe that there is a high similarity between the true phase image and the generated phase images. For quantifying the similarity, we have measured the structural similarity index measure (SSIM) value. The predicted phase images for both epoch 30 and 90 have roughly the same SSIM value (0.9140 for epcoch 30 and 0.9193 for epoch 90). On the other hand, the SSIM value is significantly lower for the predicted phase image in epoch 60 (being a value of 0.7233). Nonetheless, the trained cGAN network introduces some undesired artifacts in the generated phase images. For example, in all three epochs, a very dim ringing effect is present in the three

generated phase images. This ringing effect is not observable in the actual phase image. Also, in epoch 60, the generated phase image also shows a gridding effect, which is likely the explanation for the lower SSIM values previously stated corresponding to this epoch. Figure 5e shows line profiles from each phase image (marked in the top right corner) to highlight these artifacts. Finally, we have also observed a hazy white border on the generated phase images.

CONCLUSIONS

Digital Holographic Microscopy (DHM) is one of the most common quantitative phase imaging (QPI) methods used by the biomedical community, allowing to image 3-D label-free live cells using a single image. All DHM systems require that the recorded image (called hologram) needs to be computationally reconstructed into a accurate quantitative phase image. Among the different optical configurations, off-axis DHM systems operating in a non-telecentric regime are the most common systems. The main limitation of non-telecentric-based DHM systems is that the reconstructed phase image after filtering the object spectrum from the hologram and compensating the interference angle is distorted by a spherical phase factor introduced by the optical configuration. This spherical phase factor makes the non-telecentric DHM systems shift variant imaging systems, requiring additional computational approaches for its precise removal. This study aimed to use learning-based method to automatically reconstruct holograms captured by DHM systems operating in non-telecentric regime. The learning-based model should be able to filter the object spectrum from the hologram spectrum, compensate the interference angle between the object and reference waves, and correct the unwanted spherical phase term. To accomplish this task, we simulated a dataset of holograms recorded using a non-telecentric Mach-Zehnder DHM system with three different separations between the aperture of the MO lens and the TL. Overall, the trained pix2pix cGAN model generates phase images with high accuracy between them and the true values.

REFERENCES

1. M. H. De la Torre I., F. M. Santoyo, J. M. Flores M., and M. del Socorro Hernandez-M., "Gabor's holography: seven decades influencing optics," Appl. Opt. **61**, B225-B236 (2022)
2. M.K. Kim, "Digital Holographic Microscopy. Principles, techniques, and Applications," *Springer Series in Optical Sciences*. (Springer, 2011).
3. X. Yu, J. Hong, C. Liu and M.K. Kim. "Review of digital holographic microscopy for three-dimensional profiling and tracking," *Opt Eng*. (2014).
4. Y.K. Park, C. Depeursinge, and G. Popescu, "Quantitative phase imaging in biomedicine," *Nat Photonics.* **12**(10), 578–89 (2018).
5. B. Javidi, *et al*., "Roadmap on digital holography," *Opt. Express*. **29**(22): 35078-35118 (2021).
6. E. Cuche, P. Marquet, and C. Depeursinge, "Simultaneous amplitude-contrast andquantitative phase-contrast microscopy bynumerical reconstruction of Fresnel off-axisholograms," *Appl. Opt.* **38**, 6994-7001 (1999).
7. T. Colomb, *et al*. "Numericalparametric lens for shifting, magnification, and complete aberration compensation in digital holographic microscopy." *J. Opt. Soc. Am*. **23**(12), 3177-3190 (2006).
8. A. Doblas, E. Sánchez-Ortiga, M. Martínez-Corral, G. Saavedrax, P. Andrés, J. Garcia-Sucerquia, "Shift-variant digital holographic microscopy: inaccuracies in quantitative phase imaging," in *Opt Lett.* (2013), **38**(8), pp. 1352–1354.
9. A. Doblas, *et al*, "Accurate single-shot quantitative phase imaging of biological specimens with telecentric digital holographic microscopy," *J Biomed Opt*. **19**(4), 46022 (2014).
10. J. Min, *et al,* "Simple and fast spectral domain algorithm for quantitative phase imaging of living cells with digital holographic microscopy," *Optics Letters*, **42**(2), 227–230 (2017). https://doi.org/10.1364/ol.42.000227.
11. R. Castaneda, C. Trujillo, and A. Doblas, "Video-Rate Quantitative Phase Imaging Using a Digital Holographic Microscope and a Generative Adversarial Network," *Sensors*, **21**(23), pp. 8021, (Dec. 2021), doi: 10.3390/s21238021.
12. E. Cuche, P. Marquet, and C. Depeursinge. "Spatial filtering forzero-order and twin-image elimination in digital off-axis holography,"*Appl. Optics*, **39**,4070–4075 (2000).
13. Kinome Atlas: The Cell Image Library. *Center of Research in Biological*. Accessed on: April 28, 2022. [Online] Available: http://cellimagelibrary.org/pages/kinome_atlas

14. T. Colomb, J. K¨uhn, F. Charriere, and C. Depeursinge. “Total aberrations compensation in digital holographic microscopy with a reference conjugated hologram,” *Opt. Express*, **14**, 4300–4306 (2006).
15. J. Di, J. Zhao, W. Sun, H. Jiang, and X. Yan. “Phase aberration compensation of digital holographic microscopy based on least squares surface fitting,” *Opt. Commun*., **282**, 3873–3877 (2009).
16. K. W. Seo, Y. S. Choi, E. S. Seo, and S. J. Lee, “Aberration compensation for objective phase curvature in phase holographic microscopy,” *Opt. Letters*, **37**, 4976–4978 (2012).
17. P. Ferraro, S. De Nicola, A. Finizio, G. Coppola, S. Grilli, C. Magro, and G. Pierattini, “Compensation of the inherent wave front curvature in digital holographic coherent microscopy for quanti-tative phase-contrast imaging,” *Appl. Optics*, **42**, 1938 (2003).
18. C. J. Mann, L. Yu, C.-M. Lo, and M. K Kim, “High-resolutionquantitative phase-contrast microscopy by digital holography,” *Opt. Express*, **13**, 8693–8698 (2005).
19. P. Isola, *et al*, “Image-to-image translation with conditional adversarial networks,” *IEEE Conference on Computer Vision and Pattern Recognition (CVPR)* (2017).
20. O. Ronneberger, P. Fiscer, and T. Brox, “U-Net Convolutional Networks for Biomedical Image Segmentation. International Conference on Medical image computing and computer-assisted intervention,” *Cham*. (Springer, 2015), 234-241. https://arxiv.org/abs/1505.04597.